

PAPER • OPEN ACCESS

A robust, high-flux source of laser-cooled ytterbium atoms

To cite this article: E Wodey *et al* 2021 *J. Phys. B: At. Mol. Opt. Phys.* **54** 035301

View the [article online](#) for updates and enhancements.

You may also like

- [A Zeeman slower for diatomic molecules](#)
M Petzold, P Kaeberl, P Gersema *et al.*
- [Toward improved loading, cooling, and trapping of molecules in magneto-optical traps](#)
T K Langin and D DeMille
- [Zeeman slowers for strontium based on permanent magnets](#)
Ian R Hill, Yuri B Ovchinnikov, Elizabeth M Bridge *et al.*

A robust, high-flux source of laser-cooled ytterbium atoms

E Wodey , R J Rengelink , C Meiners, E M Rasel and D Schlippert* 

Leibniz Universität Hannover, Institut für Quantenoptik, Welfengarten 1, 30167 Hannover, Germany

E-mail: schlippert@iqo.uni-hannover.de

Received 13 October 2020, revised 25 November 2020

Accepted for publication 11 December 2020

Published 9 February 2021



Abstract

We present a high-flux source of cold ytterbium atoms that is robust, lightweight and low-maintenance. Our apparatus delivers 1×10^9 atoms s^{-1} into a 3D magneto-optical trap without requiring water cooling or high current power supplies. We achieve this by employing a Zeeman slower and a 2D magneto-optical trap fully based on permanent magnets in Halbach configurations. This strategy minimizes mechanical complexity, stray magnetic fields, and heat production while requiring little to no maintenance, making it applicable to both embedded systems that seek to minimize electrical power consumption, and large scale experiments to reduce the complexity of their subsystems.

Keywords: atom cooling and trapping, atomic beams, Zeeman slowing

(Some figures may appear in colour only in the online journal)

1. Introduction


Neutral alkaline-earth-like cold atoms are a versatile resource for quantum sensing and metrology. Besides providing the most stable frequency references [1], the availability of long-lived metastable states also allows for novel coherent matter-wave optics [2–4]. However, applications like gravitational wave detection with atoms [5] or atomic tests of the universality of free fall [6] require reliable methods for the fast production of large cold atomic samples in order to minimize noise and aliasing effects, and thus maximize the metrological gain [7].

We present a robust, lightweight, and low-maintenance source of slow ytterbium atoms that delivers 1×10^9 atoms s^{-1} into a three-dimensional magneto-optical trap (3D-MOT), comparable to state-of-the-art strontium [8] and ytterbium [9] systems. However, in contrast to the electromagnets used in these devices, our setup exclusively uses permanent magnets in Halbach configurations [10, 11] for the gener-

ation of magnetic fields. This makes our apparatus simple to assemble, lightweight, and almost maintenance-free while keeping a minimal power footprint as it requires neither high-power electrical circuits nor water cooling. Our strategy also suppresses magnetic stray fields by construction and eliminates hot atoms from the main experimental chamber, adding up to a beam apparatus suitable for high-accuracy atom interferometry or other precision experiments with cold atoms.

Our setup is depicted in figure 1. We describe and characterize its four distinct elements in the following sections. First, a hot atomic beam is produced from metallic ytterbium chunks in an oven terminated by a microchannel nozzle (section 2). We carefully study the properties of the atomic beam as they crucially determine the performance of the subsequent cooling stages and give insights on the scalability of our apparatus. Next, we present a spin-flip Zeeman slower with permanent magnets in Halbach configuration which reduces the mean forward velocity in the atomic beam (section 3). A 2D-MOT (section 4) follows and serves as a deflection and recollimation stage, preventing the residual fast atoms from entering the main experimental chamber without introducing in-vacuum moveable parts. Finally, we capture the slowed atoms in a 3D-MOT, demonstrating the usability and performance of our apparatus (section 5).

* Author to whom any correspondence should be addressed.

 Original content from this work may be used under the terms of the [Creative Commons Attribution 4.0 licence](https://creativecommons.org/licenses/by/4.0/). Any further distribution of this work must maintain attribution to the author(s) and the title of the work, journal citation and DOI.

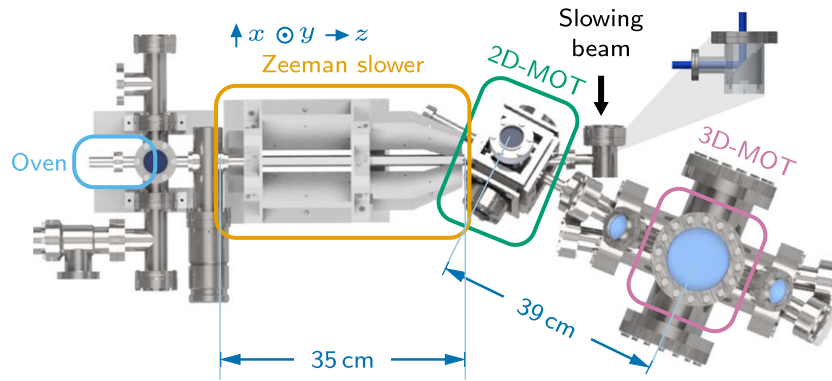


Figure 1. Overview of our cold ytterbium apparatus. An atomic beam is produced from metallic ytterbium chunks heated in an oven with a microchannel nozzle. The combination of a Zeeman slower and 2D-MOT slows down, redirects, and recollimates the atomic beam for delivery in a 3D-MOT.

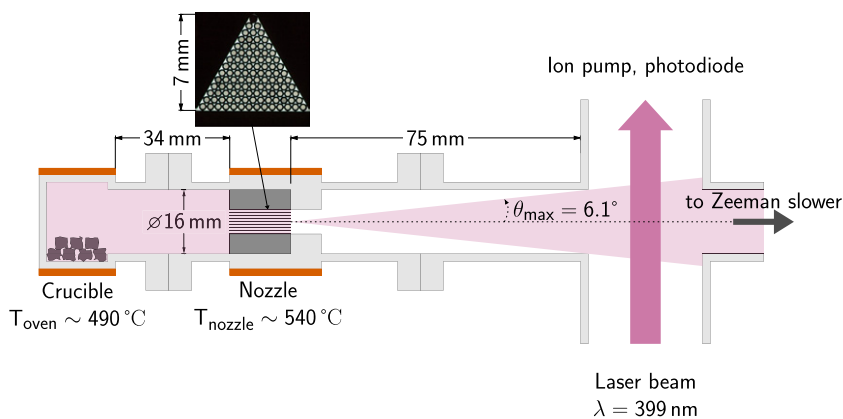


Figure 2. Sketch of the ytterbium beam apparatus. Solid ytterbium chunks are heated to $T_{\text{oven}} = 490 \text{ }^\circ\text{C}$ to form partial ytterbium vapor at 2×10^{-2} mbar using circular band heaters (depicted in red). A directed beam is extracted by a nozzle made of 104 large length-to-diameter ratio tubes (inset: photograph of the microchannel stackup with homogeneous backlight). The properties of the atomic beam (flux, divergence) are measured around 100 mm downstream the nozzle by means of laser absorption spectroscopy near the $^1\text{S}_0 \rightarrow ^1\text{P}_1$ resonance at 399 nm.

2. Oven with microchannel nozzle

2.1. Design

Figure 2 shows the design of our ytterbium oven. Solid metallic chunks (natural isotopic abundance, approximate chunk volume 10 mm^3) are vaporized in a cylindrical vacuum chamber with 19 mm inner diameter. The atomic beam is created by a nozzle made of $N_{\text{tubes}} = 104$ AISI 316L stainless-steel microchannels with inner diameter $2a = 280 \text{ }\mu\text{m}$ and outer diameter $320 \text{ }\mu\text{m}$ cut to length $L = 12 \text{ mm}$. The microchannels are assembled in a quasi-hexagonal lattice constrained by a triangular holder (inset of figure 2) which minimizes spurious apertures larger than the microchannel diameter [12]. The crucible and nozzle are heated using mineral insulated band heaters fitted to the vacuum chamber (red elements in figure 2). We require 55 W of electrical power to maintain a crucible temperature $T_{\text{oven}} = 490 \text{ }^\circ\text{C}$ and a nozzle temperature of $530 \text{ }^\circ\text{C}$ which avoids clogging the microchannels. A pressure of approximately 1×10^{-8} mbar at the nozzle outlet is maintained by a 30 L s^{-1} ion pump.

2.2. Ytterbium atomic beam

We determine the divergence and flux of the atomic beam using laser absorption spectroscopy on the $^1\text{S}_0 \rightarrow ^1\text{P}_1$ resonance at 399 nm (figure 2, inset figure 3). We use a low saturation ($s = I/I_{\text{sat}} = 0.3$) laser probe of $1/e^2$ diameter $2r_b = 7.5 \text{ mm}$ directed perpendicular to the atomic beam, around 10 cm after the nozzle. Figure 3 shows a typical laser absorption spectrum $d_0(\nu)$. The six main features correspond to nine resonances in bosonic (^{170}Yb , ^{172}Yb , ^{174}Yb , ^{176}Yb) and fermionic (^{171}Yb ($F' = 1/2, F' = 3/2$), ^{173}Yb ($F' = 3/2, F' = 5/2, F' = 7/2$)) ytterbium [13]. The stable boson ^{168}Yb cannot be resolved due its low natural abundance (0.3%) and signal-to-noise ratio limitations in this setup.

To obtain quantitative information about the atomic beam, we adjust the sum of nine Lorentzian profiles of full width at half maximum $\Gamma + 2\tilde{\sigma}$ to the absorption spectra. $\Gamma = 29 \text{ MHz}$ is the natural width of the $^1\text{S}_0 \rightarrow ^1\text{P}_1$ electronic transition and $\tilde{\sigma}$ quantifies the spectral broadening that results from residual velocity components along the probe laser beam. We found a Lorentzian shape to fit the data better than a Gaussian or Voigt profile. In the adjustment, the spectral positions of the

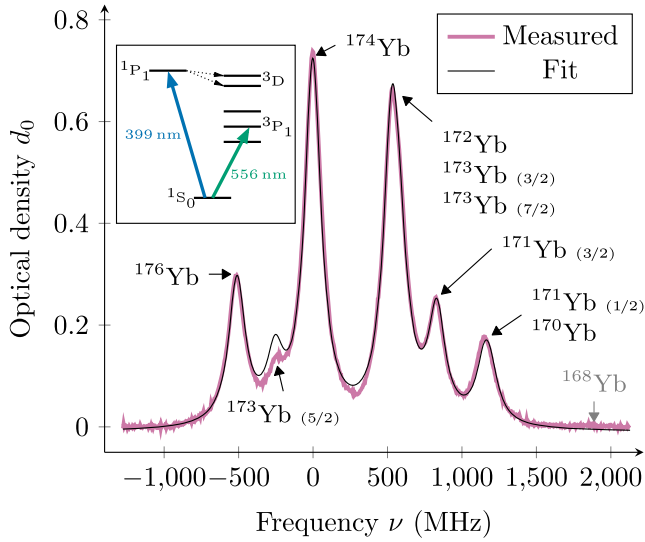


Figure 3. Laser absorption spectrum recorded around the $^1S_0 \rightarrow ^1P_1$ resonance at 399 nm in atomic ytterbium. The laser probe beam is perpendicular to the atomic beam (see figure 2), such that the spectral width results from the natural (Γ) and transverse Doppler (σ) widths. We identify six main features, corresponding to nine electronic transitions. For fermions, the number in parentheses indicates the total atomic angular momentum F in the excited state. The boson ^{168}Yb is not resolved due to its low natural abundance. Inset: simplified energy level diagram for bosonic atomic ytterbium.

features as well as their relative amplitudes are fixed, respectively set from tabulated values [14], and calculated from the isotopic natural abundances and standard L - S coupling theory [15]. For the spectrum in figure 3, we find $\bar{\sigma} = 53$ MHz which corresponds to a transverse velocity $\bar{v}_t = 21$ m s $^{-1}$ or a half-opening angle $\bar{\theta}_{1/2} = 69$ mrad.

We estimate the atomic flux for all isotopes by spectrally integrating absorption spectra. Normalizing by the spectrally-integrated scattering cross-section gives the linear density of atoms along the absorption column. Multiplying the column density by the absorption surface πr_b^2 leads to the instantaneous number of atoms N_{atoms} in the overlap volume of the laser and atomic beams:

$$N_{\text{obs}} = \frac{\int_{-\infty}^{\infty} d_0(\nu) d\nu}{\int_{-\infty}^{\infty} \frac{\sigma_0}{1+4[(2\pi\nu)/\Gamma]^2} d\nu} \times \pi r_b^2, \quad (1)$$

where $\sigma_0 = 3\lambda^2/(2\pi) \approx 0.08$ μm^2 is the on-resonance scattering cross section [16]. For a probe beam perpendicular to the atomic beam, the transit time of atoms with longitudinal velocity \bar{v} is on the order of $2r_b/\bar{v} \approx 25$ μs . If the probe beam is large enough to intersect the entire atomic beam, the total flux of atoms emerging from the oven is

$$\dot{N} = N_{\text{obs}} \times \frac{\bar{v}}{2r_b}, \quad (2)$$

where we estimate \bar{v} by averaging over a Maxwell–Boltzmann distribution at the crucible temperature T_{oven} .

Figure 4 shows the variation of flux with the crucible temperature T_{oven} . At our typical operation temperature of 490 $^{\circ}\text{C}$, the flux of ytterbium atoms passing the spectroscopy zone exceeds 2×10^{14} at s $^{-1}$.

2.3. Discussion

The fit to the spectrum in figure 3 implies that the atomic beam diverges with a half-angle $\bar{\theta}_{1/2} \approx 70$ mrad, much larger than the angle predicted from the collisionless theory for the microchannel nozzle [17, 18] $\theta_{1/2} = 1.68a/L \approx 20$ mrad. This suggests a non-negligible influence of interatomic collisions in the nozzle.

At $T_{\text{oven}} = 490$ $^{\circ}\text{C}$, the vapor pressure of ytterbium is around 2×10^{-2} mbar [19]. Assuming an ideal gas, the corresponding density is $n_0 \approx 2.2 \times 10^{20}$ at m $^{-3}$ and the mean velocity $\bar{v} \approx 300$ m s $^{-1}$. Approximating the interatomic scattering cross-section by the effective atomic diameter of ytterbium $\bar{\sigma} \approx 400$ pm, we find an average mean free path for atoms inside the nozzle [17] $\bar{\Lambda} = 11$ mm at $T_{\text{oven}} = 490$ $^{\circ}\text{C}$, which is indeed on the order of the microchannels' length $L = 12$ mm. At $T_{\text{oven}} = 450$ $^{\circ}\text{C}$ however, $\bar{\Lambda} = 36$ mm and $\bar{\Lambda} = 5$ mm for $T_{\text{oven}} = 520$ $^{\circ}\text{C}$. Since $\bar{\Lambda}$ is a monotonous function of temperature, this indicates a change of regime across the temperature range in figure 4, from transparent ($\bar{\Lambda} \gg L$) to opaque ($\bar{\Lambda} \ll L$) channels.

Giordmaine and Wang [17] derive atomic beam angular distributions $J(\theta)$ for both regimes. The total flux follows by integration over the forward half solid angle. However, according to figure 2, the vacuum tubing between the nozzle piece and the spectroscopy region truncates the atomic beam's solid angle at the spectroscopy zone to a polar angle $\theta_{\text{max}} = 6.1^{\circ}$. The prediction for the flux measured by absorption spectroscopy therefore reads:

$$\dot{N} = 2\pi \int_0^{\theta_{\text{max}}} J(\theta) \sin \theta d\theta. \quad (3)$$

The solid and dotted lines in figure 4 correspond to this model. At the highest temperature probed, the average mean free path is less than half the length of the microchannels. Nevertheless, the collisionless model (dotted line) still qualitatively reproduces the data better than the opaque source model (dashed line). The truncation represents a loss of flux of around an order of magnitude but the geometric acceptance angle of the full Zeeman slower, around 20 mrad, is far smaller than θ_{max} and therefore constitutes the major constraint on useable flux.

Despite the qualitative agreement for the total flux, the theoretical prediction does not match the observed half-width $\bar{\theta}_{1/2}$ quantitatively. The half angle divergence in the collisionless theory is around 20 mrad and above 100 mrad in the opaque theory, compared to measured values between 60 mrad and 80 mrad, which are due to the mixed regime in which we operate the nozzle. The inset in figure 4 shows some evidence for the opaque regime at higher temperatures where the beam half-

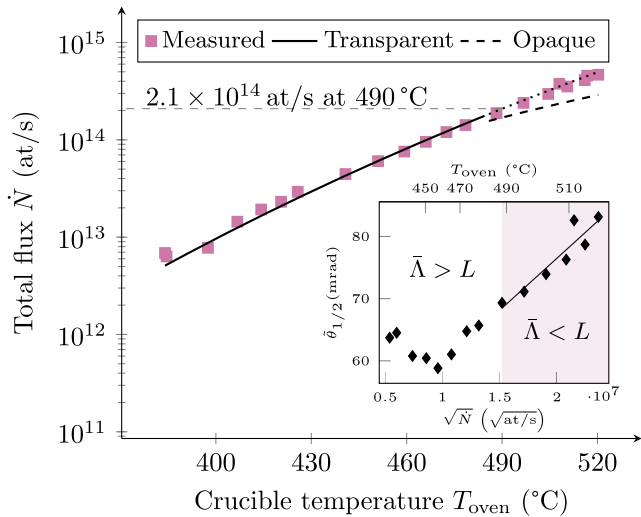


Figure 4. Flux of ytterbium atoms \dot{N} emerging from the microchannel nozzle versus crucible temperature T_{oven} . Experimental points are derived from absorption spectra applying equation (2). The solid line corresponds to equation (3), truncated at θ_{max} (see figure 2). The dotted line continues that model for temperatures above 485 °C where the average mean free path $\bar{\lambda}$ is smaller than the microchannel length L . The dashed curve corresponds to the opaque source model. Inset: onset of the interacting regime. When $\bar{\lambda} \lesssim L$, the spectral half-width $\theta_{1/2}$ scales linearly with the square-root of the measured flux [17].

width scales with the square root of the total flux, while it is predicted to be independent of flux in the transparent regime. Nevertheless, the truncation of the atomic beam by the vacuum chamber prevents a faithful observation of the angular distribution, although not limited by a thin aperture as in other work [20].

The performance of the cold atoms source strongly depends on the flux and divergence of the atomic beam exiting the oven. While the former translates into loading rate into a 3D trap, the latter accounts for the largest losses along the Zeeman slower (section 3.3). In the opaque nozzle regime, these properties are correlated, leading to a design trade-off. An increase in flux can be obtained either by rising the crucible temperature or by enlarging the nozzle diameter, a combination of microchannel diameter and count. On the one hand, increasing the nozzle diameter leads to a larger transverse size of the atomic beam, thus requiring quadratically more optical power in a Zeeman slowing beam for constant saturation conditions. On the other hand, rising the crucible temperature reaches towards the opaque nozzle regime observed in figure 4, unless the microchannel length is decreased, which, at constant aspect ratio, is limited by the availability of small diameter microchannels and clogging risks. Complementarily, optical recollimation can be used to counter beam divergence, at the expense of high laser power requirements [8]. Alternatively, novel nozzle designs [21] potentially enable higher collimation without additional laser power and better recycle atoms

with highly diverging trajectories, thus increasing the oven’s lifetime.

3. Permanent magnet Zeeman slower in Halbach configuration

We employ Zeeman slowing to bring the average atomic forward velocity $\bar{v} \approx 300 \text{ m s}^{-1}$ at the exit of the nozzle down to the few tens of m s^{-1} capture velocity of our 2D-MOT. We focus on the most abundant isotope, ^{174}Yb .

We briefly review elements of Zeeman slowing theory and motivate our design parameters in section 3.1. We then describe our permanent magnet layout in depth and characterize its magnetic properties (section 3.2). Finally, we evaluate the performance of the slower on the atomic beam (section 3.3).

3.1. Zeeman slower design

The theory of Zeeman slowing is extensively covered in the literature [16, 22]. We consider atoms of mass m addressed on a cycling transition of width Γ and effective magnetic moment $\bar{\mu}$ with light of wavenumber k detuned by Δ from the atomic resonance. The ideal field profile to decelerate atoms from a capture velocity v_c at a constant rate $\eta a_{\text{max}} = \eta (\hbar k \Gamma / 2m)$, $0 < \eta < 1$, reads:

$$B(z) = \begin{cases} B_0 + B_L \cdot \sqrt{1 - \frac{z}{L_{\text{stop}}}} & 0 < z < L \\ 0 & \text{otherwise,} \end{cases} \quad (4)$$

where $L_{\text{stop}} = v_c^2 / (2\eta a_{\text{max}})$ is the length required to stop the atoms in the v_c velocity class. The field profile is truncated at $L = L_{\text{stop}} - v_c^2 / (2\eta a_{\text{max}}) < L_{\text{stop}}$ to be able to extract atoms at a non-zero velocity v_e .

The design degrees of freedom are the field offset $B_0 = \hbar \Delta / \bar{\mu}$, and the amplitude $B_L = \hbar k v_c / \bar{\mu}$. The field varies from $B_0 + B_L$ at $z = 0$ to $B_0 + \hbar k v_e / \bar{\mu}$ at $z = L$. The exit velocity v_e can be experimentally tuned either by adjusting the magnitude of the field near the end of the slower, or by varying the detuning Δ , such that the slower can in practice be designed for L_{stop} .

Table 1 summarizes the design parameters for our Zeeman slower operating on the $^1S_0 \rightarrow ^1P_1$ ($m_J = -1$) transition in ^{174}Yb . We choose the capture velocity $v_c = 390 \text{ m s}^{-1}$, which corresponds to around 75% of the atoms in the beam with a forward velocity below the slowing threshold. The minimal slower length is 14 cm ($\eta = 1$). To make the design less critical, we choose $L_{\text{stop}} = 30 \text{ cm}$ ($\eta \approx 0.5$). The detuning Δ determines the offset B_0 and hence the magnitude of the maximum field to generate. Minimizing this quantity would lead to the choice $B_0 = -B_L/2$, that is $\Delta = -490 \text{ MHz}$. However, for geometrical reasons, the Zeeman slowing laser beam passes through, or very close to, the center of the subsequent 2D-MOT, which could become unbalanced or lifetime-limited

Table 1. Zeeman slower design parameters

Parameter	Symbol	Value
Angular momentum change	$\tilde{\mu}$	$-1.035 \cdot \mu_B \approx -14 \text{ MHz mT}^{-1}$
Maximum deceleration	$-a_{\text{max}} = -\frac{\hbar k \Gamma}{2m}$	$-5.3 \times 10^5 \text{ m s}^{-2}$
Detuning	Δ	-700 MHz
Capture velocity	v_c	390 m s^{-1}
Length	L_{stop}	30 cm
Deceleration margin	$\eta = \frac{v_c^2}{2L_{\text{stop}}a_{\text{max}}}$	0.48
Saturation parameter	$s = \frac{\eta}{1-\eta}$	0.93
Field amplitude	$B_L = \frac{\hbar k v_c}{\tilde{\mu}}$	-67 mT
Field offset	$B_0 = \frac{\hbar \Delta}{\tilde{\mu}}$	48 mT

through excessive losses to the ^3D states (see inset figure 3) with too near-resonant light. To rule out this scenario, we choose $\Delta = -700 \text{ MHz}$, which corresponds to a loss time constant above 200 s [23]. Also, the influence of the Zeeman slowing beam on the scattering rate is more than 1000 times smaller than that of the 2D-MOT beams. The magnetic field profile corresponding to equation (4) with the parameters in table 1 is shown as the solid green line in the middle panel in figure 5.

3.2. Zeeman slowing field from permanent magnets in Halbach array configuration

We use permanent magnets in a Halbach configuration to produce the magnetic field described by equation (4) and the parameters in table 1. Halbach arrays are particular magnetic configurations that produce magnetic multipole fields in a well constrained domain in space, while suppressing the field outside this region [24]. We consider a thin magnetic cylinder whose local magnetization $\mathbf{M}(\phi)$ stays orthogonal to the cylinder's axis and rotates as:

$$\frac{\mathbf{M}}{|\mathbf{M}|} \equiv \hat{e}_M = \cos(2\phi) \hat{e}_\rho + \sin(2\phi) \hat{e}_\phi. \quad (5)$$

where (ρ, ϕ, z) are cylindrical coordinates with z along the cylinder's axis. Near the cylinder's axis, the sum magnetic field is purely transverse and aligns with the $\phi = 0$ direction (\hat{e}_y in figure 5). Outside of the cylinder, the produced field is theoretically zero. Other permanent magnet arrangements can produce longitudinal fields, at the expense of larger stray fields since the Halbach symmetry is not maintained [25]. If the magnetic object is not a cylinder but a cone, the magnitude of the transverse field decreases with increasing cone radius, however also introducing a longitudinal field component except on the cone's axis. We assert numerically, as already shown in previous work [10, 11], that a Halbach cone produces a percent-level approximation of the ideal Zeeman slowing field from equation (4).

Since a continuous magnetic material with the magnetization rotation described by equation (5) is not practical, and similarly to the work in references [10, 11], we discretize the array using an eight-fold symmetry. However, contrary to previous work, our design exhibits a zero crossing and a higher overall

average gradient (200 mT m^{-1} versus 120 mT m^{-1} for reference [11], and 33 mT m^{-1} for reference [10]). In particular, the large magnetic gradient increases the magnitude of the field's longitudinal component due to the imperfect continuity of the Halbach pattern, which may impact slowing performance.

The top panel in figure 5 shows the construction of our magnet. The main field is generated by two sets of eight NdFeB rectangular cuboids¹ with length 128 mm , $6 \text{ mm} \times 6 \text{ mm}$ square cross-section, and nominal remanence $B_r = 1.08 \text{ T}$, magnetized along one of the transverse directions. These long cuboids are arranged in two Halbach cones with slopes $+9.6^\circ$ and -24° . We additionally use $8 \times 4 = 32$ smaller rectangular cuboids ($25 \text{ mm} \times 4 \text{ mm} \times 4 \text{ mm}$, $B_r = 1.17 \text{ T}$ ²) as adjustment variables to better fit the starting field, the zero-field transition regime in the middle of the slower, and help decreasing the field faster at the exit of the slower. We numerically optimize the positions and orientations of all the permanent magnets based on an analytic model for the magnets' field [10], while enforcing the Halbach symmetry. The optimized configuration corresponds to the solid black curve in the middle panel in figure 5.

The full magnet therefore consists of eight sets of six magnets clamped between aluminum plates (clear bodies in figure 5). The positions of the magnets on the plates is engraved (e.g. 3 mm deep per plate for the long magnets) during the manufacturing process. The assembly of the magnet takes less than 2 h , dominated by the identification of the magnetization direction for the 48 permanent magnets. We kept the manufacturing tolerances below 0.5 mm to constrain the assembly sufficiently while taking size variations of the individual magnets into account. The plates are pressed against each other using five M3 bolts and mounted in octagonal fixtures (dark bodies in figure 5) to obtain the desired configuration. The total weight of this assembly is 10 kg . We measure the magnetic field along the magnet's axis using a 3-axes teslameter³. As shown in figure 5 (middle panel: blue triangles), we reproduce the calculated field (solid black line) to around 10% (lower panel). In the transverse direction, the field decays to background values within 10 cm outside the magnet assembly.

¹ HKCM Engineering, part no. Q128x06x06Zn-30SH.

² HKCM Engineering, part no. Q25x04x04Zn-35H.

³ F W Bell, Model 7030.

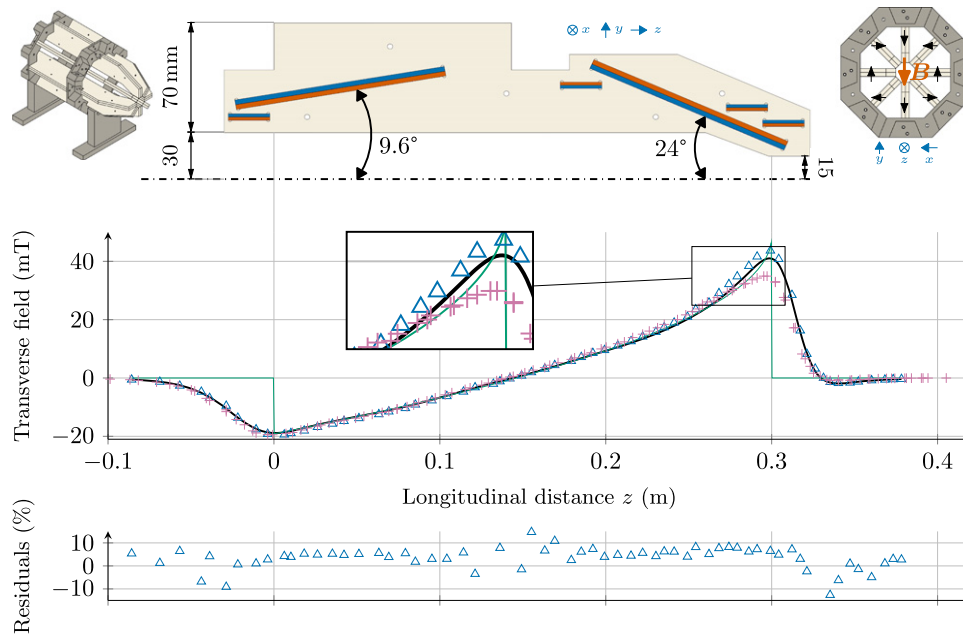


Figure 5. Construction and magnetic field of the permanent magnets-based Zeeman slower. Top: mechanical arrangement of the two main magnets and four trimmer magnets (red: north pole, blue: south pole) in one of the eight plates forming the magnet assembly. The dash-dotted line corresponds to the axis of the slower’s vacuum pipe (not represented). The drawing is horizontally aligned with the graphs below. *Inset left:* 3D rendering of the assembled magnet with the eight plates containing the magnets (clear) and their mounting fixtures (dark). *Inset right:* transverse view of the magnet assembly looking in the $+\hat{e}_z$ direction. The black arrows show the magnetization direction for the entrance trimmer magnet on all eight plates, effectively forming an eight-fold discrete Halbach configuration that locally generates a transverse magnetic field along $-\hat{e}_y$ (red arrow). Middle: ideal (—), calculated (---), and measured (Δ , +) strong transverse component of the magnetic field along the slower’s magnet. + represents the externally trimmed configuration used for loading the 2D-MOT of section 4. Bottom: residuals of the measurements (Δ) to the corresponding calculated configuration (—). Most points lie within 10% of the numerical model.

3.3. Slowing performance

Our design achieves slowing by scattering photons on the $^1S_0 \rightarrow ^1P_1$ ($m_J = -1$) transition, which is a σ^- ($\Delta m_J = -1$) transition. However, since the magnetic field is transverse to the light propagation direction, the configuration maximizing the circularly-polarized light content as seen by the atoms corresponds to light polarized linearly along \hat{e}_x , perpendicular to the magnetic field direction \hat{e}_y (see top panel of figure 5). This implies that only half of the optical power has the correct handedness to drive the σ^- transition and thus to contribute to the dominant slowing effect. The σ^+ polarization component is resonant with the atoms at some positions in the slower but this does not affect overall performance. An influence via coherent population dynamics is ruled out by the non-magnetic 1S_0 ground state. The slowing beam has a $1/e^2$ diameter of 4 mm and total power of 80 mW resulting in a peak intensity of $3.2 \times 10^2 \text{ mW cm}^{-2}$ ($\approx 2.7 \times I_{\text{sat}}$ with σ^- polarization). After several months of operation and evaporating around 100 mg of ytterbium from the crucible, we observe no degradation of performance that could be traced back to long-term reflectivity losses of the in-vacuum mirror used to couple the slowing beam into the chamber [26] (see figure 1).

We characterize the slowed atomic beam using absorption spectroscopy under a 30° angle at the exit of the slower. Figure 6 shows the longitudinal velocity profile for ^{174}Yb atoms. The capture velocity around 390 m s^{-1} is clearly

visible, as well as the collection of low velocity ($< 50 \text{ m s}^{-1}$) atoms. We maximize the flux of slow atoms by adjusting the laser detuning to the $^1S_0 \rightarrow ^1P_1$ transition and tuning the magnetic field with two additional trimming bar magnets placed symmetrically at the exit of the magnet assembly. The resulting field is plotted using pink crosses in the middle panel in figure 5. The main effect of these extra trimmers is to avoid significantly overshooting the ideal magnetic field profile, thus keeping the local deceleration parameter η close to its design value and therefore avoid losing atoms from the slowing profile due to missing light intensity.

For the data presented in figure 6, the detuning is $\Delta = -580 \text{ MHz}$, 4Γ away from the design value -700 MHz . This is caused by the decrease in field magnitude due to the external trimmers, and the need for a finite exit velocity. The most probable exit velocity in figure 6 is $v_e = 15 \text{ m s}^{-1}$. We measured a trimmed field maximum of 35 mT, which matches the prediction from equation (4) $\hbar\Delta/\tilde{\mu} + \hbar kv_e/\tilde{\mu} = 37 \text{ mT}$.

Ideally, all atoms below the capture velocity should be slowed down. This is evidently not the case in figure 6, mainly due to the divergence of the atomic beam inside the slower. Atoms travelling too far off-axis are not interacting with the slowing beam and therefore not decelerated further. This effect is amplified with decreasing velocity since the longitudinal velocity becomes comparable to the transverse one. Increasing the slowing beam diameter or decreasing the atomic beam

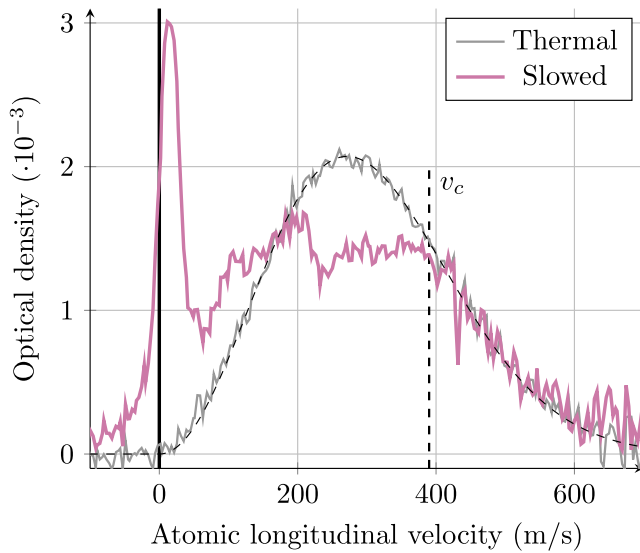


Figure 6. Absorption spectroscopy of the atomic beam under a 30° angle at the exit of the Zeeman slower. The resulting spectrum shows the longitudinal velocity distribution and the effect of the slowing laser beam. Atoms exiting the oven with a velocity below $v_c \approx 390 \text{ m s}^{-1}$ are slowed down to below 50 m s^{-1} . The frequency axis is calibrated using a simultaneous spectroscopy measurement under an axis perpendicular to the atomic beam. The dashed curve is a fit to the thermal velocity distribution by a Maxwell–Boltzmann function at $T_{\text{oven}} = 450 \text{ }^\circ\text{C}$.

divergence with radiation pressure prior to the Zeeman slower [8] can effectively mitigate this issue, at the cost of increased optical power requirements.

4. 2D-MOT recollimation/deflection stage

Constraints on geometry of the main experimental chamber for this atomic source dictate a minimum distance of several tens of centimeters between the exit of the Zeeman slower and the center of the 3D trap. This would lead to a large expansion of the slow atomic beam and a low capture efficiency in the 3D trap. In order to mitigate this issue, we implement a 2D-MOT between the Zeeman slower and the 3D-MOT, effectively recollimating the atomic beam. Since the 2D-MOT is loaded under a 30° angle, only trapped atoms can enter the main experimental chamber and the trap also serves as a shutter. This also removes the need for coupling the Zeeman slowing beam through the main chamber, thus avoiding perturbing the 3D-MOT with the slowing light and reducing the complexity of the optical layout.

4.1. Design

The magnetic quadrupole field for the 2D-MOT is realized by four permanent magnet bars⁴ ($80 \text{ mm} \times 8 \text{ mm} \times 6 \text{ mm}$, $B_r = 1.17 \text{ T}$) in a square Halbach configuration with 38 mm side length. In agreement with the numerical simulation, we measured a field gradient of 5.4 mT cm^{-1} over the whole trap volume.

⁴ HKCM Engineering Q80x08x06Zn-35H.

We generate the optical radiation pressure using two retro-reflected $1 \text{ cm} \times 4 \text{ cm}$ laser beams with 40 mW each ($\approx 0.4 \times I_{\text{sat}}$) tuned 16 MHz (0.5Γ) to the red of the $^1\text{S}_0 \rightarrow ^1\text{P}_1$ resonance. Beam shaping is achieved using pairs of cylindrical lenses.

4.2. Characterization

We characterize the atomic beam produced by the 2D-MOT with retro-reflected spectroscopy in the main chamber. Since the 2D-MOT mostly affects velocity components perpendicular to its axis, the longitudinal velocity of atoms exiting the 2D-MOT corresponds to the projection of the slower's exit velocity on the 2D-MOT axis. We find a flux optimum for a 2D-MOT exit velocity $\bar{v}_l = 20 \text{ m s}^{-1}$, characterizing the trade-off between low output velocity and excessive losses due to beam divergence in the Zeeman slower.

Since the transverse velocity is not resolved in our retro-reflected spectroscopy setup, we deduce it from the size of the atomic beam in the center of the main chamber. Varying the probe beam diameter, we estimate an atomic beam diameter of 1 cm at a distance of 23 cm from the exit of the 2D-MOT. This corresponds to a maximum transverse velocity $(1 \text{ cm}/23 \text{ cm}) \cdot \bar{v}_l < 1 \text{ m s}^{-1}$ or five times the Doppler limit (0.18 m s^{-1}) and represents a factor 20 improvement over the atomic beam divergence at the exit of the oven.

The trade-off between divergence and low exit velocity is also relevant at the exit of the 2D-MOT. Indeed, the longitudinal velocity must be small enough to enable capture by the 3D-MOT, while maintaining sufficient beam collimation despite the 23 cm travel distance between the exit of the 2D-MOT and the center of the 3D-MOT. Since the transverse velocity is on the order of 1 m s^{-1} , forward velocities around 20 m s^{-1} and above are required to restrict the atomic beam diameter to the practical size of single digit centimeters.

5. Full system characterization

We characterize the overall performance of the system consisting of the oven, the Zeeman slower, and the 2D-MOT by capturing the ytterbium atoms in a large volume 3D-MOT and measuring the corresponding loading rate. This provides a realistic estimate of the useable flux for further cooling steps and removes the need for geometrical assumptions associated with spectroscopic flux measurements.

5.1. 3D-MOT

We operate the 3D MOT on the $^1\text{S}_0 \rightarrow ^1\text{P}_1$ transition. The laser beams have a $1/e^2$ diameter around 2 cm . The magnetic field gradient is produced by a pair of coils in anti-Helmholtz configuration. We determine the number of trapped atoms by absorption imaging.

We optimize the trap for loading rate and maximum atom number. We find the optimal loading performance for a detuning $\Delta = -32 \text{ MHz} \approx -1.1\Gamma$ from the $^1\text{S}_0 \rightarrow ^1\text{P}_1$ resonance, a magnetic field gradient $\delta B = 210 \text{ mT m}^{-1}$, and $P_{\text{MOT}} = 30 \text{ mW}$ per beam ($0.08 \times I_{\text{sat}}$ per beam). Figure 7 shows the loading performance. Our trap saturates at a steady-state atom number

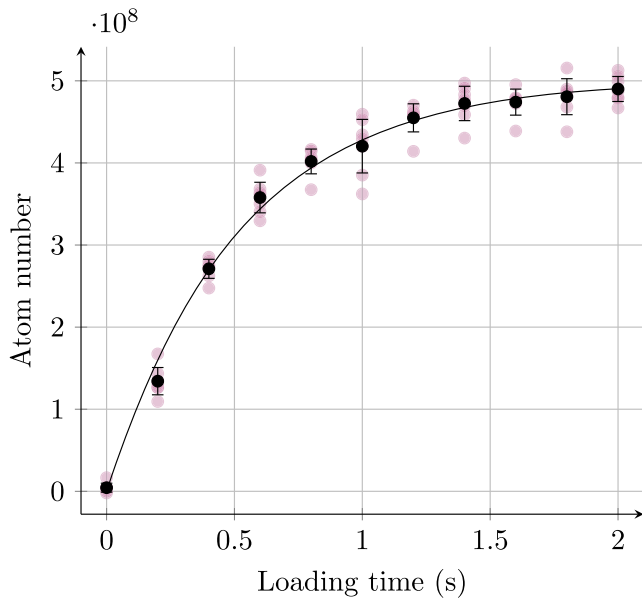


Figure 7. Loading curve of the 3D MOT. The solid line is a fit of equation (6), with best fit parameters $\gamma = 1 \times 10^9$ at s^{-1} and $R = 2/\text{s}$. The black points (\bullet) represent averages over six realizations of the loading time scan (purple points, \bullet) with error bars corresponding to the standard deviation.

of 5×10^8 atoms within about 2 s. We extract the loading rate using a one-body loss rate model:

$$N(t) = \frac{R}{\gamma} (1 - \exp(-\gamma t)), \quad (6)$$

where R is the loading rate [27]. The one-body loss rate γ contains losses due to background collisions but is dominated by radiative loss via the $^3\text{D}_{1,2}$ to the $^3\text{P}_{0,2}$ states (inset figure 3), making it highly dependent on beam intensity and detuning [28]. No significant two-body losses were observed compared to the strong one-body loss rate and are therefore neglected.

Adjusting the model of equation (6) to the data in figure 7, we find $R = 1 \times 10^9$ at s^{-1} and $\gamma = 2/\text{s}$. At higher powers the maximum loading rate remains the same but relaxes the requirements on detuning and gradient, allowing the same loading rate in a larger part of the parameter space. This behaviour suggests that in these configurations the loading rate is limited only by the flux into the main chamber and would allow for larger steady-state numbers at larger detunings and gradients as long as sufficient laser power can be provided.

5.2. System performance evaluation

Starting from a flux of 2×10^{14} at s^{-1} at the exit of the oven, our apparatus loads 5×10^8 ^{174}Yb atoms in 2 s (1×10^9 at s^{-1} initial loading rate) in a 3D-MOT on the $^1\text{S}_0 \rightarrow ^1\text{P}_1$ transition. Accounting for the natural abundance of ^{174}Yb (32%), this represents a loss of five orders of magnitude in atom numbers during the slowing, redirection, and recollimation processes.

Table 2. Flux of ^{174}Yb atoms at different positions along the beamline. The oven flux is given in figure 4 weighted by the natural abundance of ^{174}Yb . For the Zeeman slower, we distinguish between the total flux of atoms, cumulating all velocity classes, and the slowed flux, accounting only atoms with less than 50 m s^{-1} forward velocity. Finally, the captured flux is the loading rate into the 3D-MOT according to equation (6).

Position along beamline	Flux in atoms s^{-1}
Oven	6×10^{13}
Zeeman slower total	5×10^{11}
Zeeman slower ($<50 \text{ m s}^{-1}$)	6×10^9
Captured by 3D-MOT	1×10^9

Table 2 shows a summary of flux measurements performed along the beamline. The major loss contributor is the Zeeman slower. The loss of total flux, cumulating all velocity classes at the exit of the Zeeman slower's vacuum pipe, is accounted for by the slower's length (60 cm including all connection pieces and isolation valves) and the divergence of the atomic beam exiting the oven (70 mrad, see figure 4). This gives a maximum throughput of 1.3%, i.e. a maximum flux of 8×10^{11} at s^{-1} , in good agreement with the measured value of 5×10^{11} at s^{-1} . The loss of flux during the slowing process is split between the slower's velocity acceptance (25% of the atoms are above the capture velocity $v_c = 390 \text{ m s}^{-1}$) and atomic beam divergence inside the slower (see discussion in section 3), with the latter dominating largely.

Reducing the divergence of the atomic beam at the exit of the oven is therefore a promising way for improving the slowing efficiency and preserving flux along the beamline. For example, reducing the divergence half-angle by a factor 3 increases the geometric throughput by almost a factor 8 and is expected to also improve on the slowing losses. Since the oven is operated near the opaque channel regime to achieve high flux, the collimation needs to be performed optically. With our apparatus, the above recollimation would require around 150 mW of laser power which are currently not at our disposal. Improvements by simple optical collimations after the oven have been observed by experiments, for example in reference [8]. Nevertheless, when the oven nozzle is in the opaque channel regime, the divergence increases with flux, correspondingly constraining the laser system or the geometry of the optical collimation chamber. Alternatively, the slower's length could be reduced, limiting divergence effects but decreasing its safety margin η , or the slowing beam's diameter can be increased, at the expense of a considerable rise in laser power consumption.

As discussed in section 4, the current apparatus is unsuitable for direct loading of a MOT operating on the $^1\text{S}_0 \rightarrow ^3\text{P}_1$ transition [27]. This is mostly due to the size of the 3D trap chamber, constrained by other design requirements for this apparatus. In order to keep a reasonably sized MOT, the transverse velocity around 1 m s^{-1} of the atoms exiting the 2D-MOT require the forward velocity to stay above 20 m s^{-1} while not significantly sacrificing flux. In order to benefit from narrow line cooling, further optimization of the 2D-MOT stage up to the Doppler limit is a possibility. However, it is more

versatile to add an extra slowing stage in the main chamber. The most straightforward would be sequential loading via a singlet MOT but other schemes such as two-stage cooling [29] or a core-shell MOT [9] might also be considered.

6. Conclusion

We have built and characterized a source of laser-cooled ytterbium atoms delivering 1×10^9 atoms s^{-1} in a 3D magneto-optical trap. All necessary magnetic fields on the atomic beamline are produced by permanent magnets in Halbach configurations. This provides easily reproducible designs with low stray magnetic fields, as well as a high robustness since no maintenance on e.g. water cooling circuits is required. Also, the resulting assembly is lightweight and can be disassembled for investigation, vacuum bakeout, or transportation. Apart from the laser systems, the only electrical power consumption stems from the oven (<50 W) and could be further reduced using in-vacuum heating [20]. In particular, we found the use of an in-vacuum mirror for coupling the Zeeman slowing laser beam in the chamber to be an efficient alternative to the commonly used heated viewports.

Besides a Zeeman slower, our apparatus features a 2D-MOT operated as a deflection and recollimation stage. While adding little complexity, this component is crucial to keeping a high fraction of the flux exiting the Zeeman slower capturable by the subsequent 3D trap. This is in particular relevant in setups, like ours, where the main experimental chamber needs to have a large physical volume due to other design constraints, at the expense of little loss of flux.

Our study involves a detailed characterization of the atomic beam emerging from a microchannel nozzle. We confirm that systems aiming at very high fluxes operate at the onset of the opaque channel regime, where interatomic interactions inside the nozzle cannot be neglected and the atomic beam divergence increases with increasing flux. Because initial beam divergence directly impacts the performance of the Zeeman slower, we anticipate the nozzle to be a major design point for future devices aiming at even higher flux.

Overall, our apparatus operates reliably at its maximum performance level with no other maintenance than that associated with laser systems at a level comparable to that achieved in other ytterbium [9] and strontium [8] setups. Owing to the simple permanent magnet assembly, the complexity added by the Zeeman slower compared to pure 2D-MOT systems [30, 31] is minimal, while significantly increasing cold flux. This constitutes a solid starting point for complex cold atoms experiments such as, but not limited to, high-performance atom interferometers.

Acknowledgments

The authors thank M Robert-de-Saint-Vincent for insightful discussions on the microchannel nozzle and in-vacuum mirrors, A Billon for early work on the microchannel nozzle, and D Tell for careful proof-reading of the manuscript. We are grateful to C Schubert, D Tell, and K Zipfel for their contri-

butions and W Ertmer for his vision and long-lasting support towards very long baseline atom interferometry in Hannover. This work is part of the Hannover very long baseline atom interferometry facility, a major research equipment funded by the German Research Foundation (Deutsche Forschungsgemeinschaft, DFG). We acknowledge support by the Collaborative Research Centers 1128 ‘geo-Q’ and 1227 ‘DQ-mat’, and Germany’s Excellence Strategy within EXC-2123 ‘QuantumFrontiers’ (Project No. 390837967). DS acknowledges funding from the German Federal Ministry of Education and Research (BMBF) through the funding program Photonics Research Germany (Contract No. 13N14875). EW acknowledges support from ‘Niedersächsisches Vorab’ through the ‘Quantum- and Nano-Metrology (QUANOMET)’ initiative (project No. QT3).

ORCID iDs

E Wodey  <https://orcid.org/0000-0001-9522-8558>

R J Rengelink  <https://orcid.org/0000-0002-0365-1066>

D Schlippert  <https://orcid.org/0000-0003-2168-1776>

References

- [1] Ludlow A D, Boyd M M, Ye J, Peik E and Schmidt P O 2015 *Rev. Mod. Phys.* **87** 637–701
- [2] Hu L, Poli N, Salvi L and Tino G M 2017 *Phys. Rev. Lett.* **119** 263601
- [3] Plotkin-Swing B, Gochnauer D, McAlpine K E, Cooper E S, Jamison A O and Gupta S 2018 *Phys. Rev. Lett.* **121** 133201
- [4] Rudolph J, Wilkason T, Nantel M, Swan H, Holland C M, Jiang Y, Garber B E, Carman S P and Hogan J M 2020 *Phys. Rev. Lett.* **124** 083604
- [5] Loriani S et al 2019 *New J. Phys.* **21** 063030
- [6] Hartwig J, Abend S, Schubert C, Schlippert D, Ahlers H, Posso-Trujillo K, Gaaloul N, Ertmer W and Rasel E M 2015 *New J. Phys.* **17** 035011
- [7] Savoie D, Altorio M, Fang B, Sidorenkov L A, Geiger R and Landragin A 2018 *Sci. Adv.* **4** eaau7948
- [8] Yang T, Pandey K, Pramod M S, Leroux F, Kwong C C, Hajiyev E, Chia Z Y, Fang B and Wilkowski D 2015 *Eur. Phys. J. D* **69** 226
- [9] Lee J, Lee J H, Noh J and Mun J 2015 *Phys. Rev. A* **91** 053405
- [10] Cheiney P et al 2011 *Rev. Sci. Instrum.* **82** 063115
- [11] Ali D B, Badr T, Bréziillon T, Dubessy R, Perrin H and Perrin A 2017 *J. Phys. B: At. Mol. Opt. Phys.* **50** 055008
- [12] Senaratne R, Rajagopal S V, Geiger Z A, Fujiwara K M, Lebedev V and Weld D M 2015 *Rev. Sci. Instrum.* **86** 023105
- [13] Deilamian K, Gillaspay J D and Kelleher D E 1993 *J. Opt. Soc. Am. B* **10** 789
- [14] Das D, Barthwal S, Banerjee A and Natarajan V 2005 *Phys. Rev. A* **72** 032506
- [15] Degl’Innocenti E L 2014 *Atomic Spectroscopy and Radiative Processes* (Milan: Springer)
- [16] Metcalf H J and van der Straten P 1999 *Laser Cooling and Trapping* (New York: Springer)
- [17] Giordmaine J A and Wang T C 1960 *J. Appl. Phys.* **31** 463–71
- [18] Ramsey N 1956 *Molecular Beams* (Oxford: Oxford University Press)

- [19] Lide D R 1997 *Handbook of Chemistry and Physics* vol 78 (Boca Raton: CRC Press)
- [20] Schioppo M, Poli N, Prevedelli M, Falke S, Lisdat C, Sterr U and Tino G M 2012 *Rev. Sci. Instrum.* **83** 103101
- [21] Li C, Chai X, Wei B, Yang J, Daruwalla A, Ayaza F and Raman C 2019 *Nat. Commun.* **10** 1831
- [22] Phillips W D and Metcalf H 1982 *Phys. Rev. Lett.* **48** 596–9
- [23] Freytag R 2015 Simultaneous magneto-optical trapping of ytterbium and caesium *PhD Thesis* Imperial College London
- [24] Halbach K 1980 *Nucl. Instrum. Methods* **169** 1–10
- [25] Hill I R, Ovchinnikov Y B, Bridge E M, Curtis E A and Gill P 2014 *J. Phys. B: At. Mol. Opt. Phys.* **47** 075006
- [26] Huckans J, Dubosclard W, Maréchal E, Gorceix B, Laburthe-Tolra B O and Robert-de Saint-Vincent M 2018 Note on the reflectance of mirrors exposed to a strontium beam (arXiv:1802.08499)
- [27] Guttridge A, Hopkins S A, Kemp S L, Boddy D, Freytag R, Jones M P A, Tarbutt M R, Hinds E A and Cornish S L 2016 *J. Phys. B: At. Mol. Opt. Phys.* **49** 145006
- [28] Cornish J W, Lee H G, Lee S, Ahn J, Lee W K, Yu D H, Lee S K and Park C Y 2012 *Phys. Rev. A* **85** 035401
- [29] Lunden W, Du L, Cantara M, Barral P, Jamison A O and Ketterle W 2020 *Phys. Rev. A* **101** 063403
- [30] Dörscher S, Thobe A, Hundt B, Kochanke A, Le Targat R, Windpassinger P, Becker C and Sengstock K 2013 *Rev. Sci. Instrum.* **84** 043109
- [31] Barbiero M, Tarallo M G, Calonico D, Levi F, Lampoiesi G and Ferrari G 2020 *Phys. Rev. Appl.* **13** 014013